Magnetic resonance in porous media: Recent progress

Yi-Qiao Song, H. Cho, Tim Hopper, Andrew E. Pomerantz, and Phillip Zhe Sun

Citation: The Journal of Chemical Physics **128**, 052212 (2008); doi: 10.1063/1.2833581
View online: http://dx.doi.org/10.1063/1.2833581
View Table of Contents: http://scitation.aip.org/content/aip/journal/jcp/128/5?ver=pdfcov
Published by the AIP Publishing

Magnetic resonance in porous media: Recent progress

Yi-Qiao Song,[1,3,a)] H. Cho,[1,2] Tim Hopper,[1] Andrew E. Pomerantz,[1] and Phillip Zhe Sun[3]
[1]*Schlumberger-Doll Research, One Hampshire Street, Cambridge, Massaschusetts 02139, USA*
[2]*Memorial Sloan-Kettering Cancer Center, 1275 York Ave., New York, New York 10021, USA*
[3]*Athinoula A. Martinos Center for Biomedical Imaging, Department of Radiology, Massachusetts General Hospital, and Harvard Medical School, Charlestown, Massachusetts 02129, USA*

(Received 16 October 2007; accepted 17 December 2007; published online 11 February 2008)

Recent years have seen significant progress in the NMR study of porous media from natural and industrial sources and of cultural significance such as paintings. This paper provides a brief outline of the recent technical development of NMR in this area. These advances are relevant for broad NMR applications in material characterization. © *2008 American Institute of Physics*.
[DOI: 10.1063/1.2833581]

I. INTRODUCTION

NMR has become an important technique for characterizing porous materials in recent years primarily as a bulk measurement of the statistical properties of the pore space and the fluids inside. The original idea of using spin relaxation as a probe of pore space was proposed in 1970 by Senturia and Robinson.[1] In the early 1980s, two papers[2,3] reported that the spin relaxation can be used to determine the surface-to-volume ratio and its distribution in porous rocks and cements.[4,5] It has been shown that different relaxation rates reflect different pools of water in the microstructure of cement and can be used to monitor the cement hydration process. Since early 1980s, NMR has been a commercial well-logging service for oil field exploration. In early 1990s, pulsed NMR was introduced into the oil and gas industry and NMR has since become increasingly important for the evaluation of subsurface earth formations.

Characteristics of pore structure, such as the surface-to-volume ratio and tortuosity, can also be noninvasively probed by molecular diffusion.[6–9] Recent development of the internal field based technique and two-dimensional NMR of relaxation and diffusion[10–13] have proven particularly useful to characterize pore geometry.[14] In addition, the development of portable NMR sensors [e.g., NMR logging devices[4] and the NMR–mobile universal surface explorer (MOUSE) (Ref. 15)] demonstrates the potential to extend such new NMR technologies to *in situ* material characterization.

This manuscript outlines some recent developments and discusses their potential applications. However, it does not intend to provide a complete coverage of all development or an in-depth review of the theory and execution of these techniques. Readers should consult the relevant publications in order to evaluate the suitability of individual measurements for specific application.

[a)]Author to whom correspondence should be addressed. Tel.: 1-617-768-2333. FAX: 1-617-768-2386. Electronic mail: ysong@slb.com.

II. DIFFUSION-BASED TECHNIQUES

A. Dispersion

Dispersion, the transport of molecules or tracers due to combined effects of diffusion and fluid flow at low Reynolds number, is an important topic not only in fundamental hydrodynamics but also in diverse fields including biological perfusion, chemical reactors, soil remediation, and oil recovery. The probability distribution of displacements in the long time and large displacement regime is expected to become a Taylorian with a Gaussian displacement distribution whose center moves at the average velocity and whose width is given by a time-independent dispersion coefficient. de Gennes[3] suggested that such a simple picture can be "upset" in a porous medium when stagnation zones are present. However, experiments and simulations on packed spheres were not yet conclusive whether the long time dispersion is Taylorian.

Scheven *et al.* have reexamined the dispersion problem using pulsed field gradient NMR by investigating the evolution of the displacement distribution with systematically varied spatiotemporal coarse graining parameters. They have characterized the shape of the displacement distribution by its cumulant expansion using data acquired with low q (e.g., gradient) values. Here, q characterizes the wave vector for diffusion dynamics and the low q regime means that $1/q$ is longer than the typical structural length scale of the materials (e.g., grain size). These low q measurements allow them to obtain the first three moments of the displacement distribution, the mean, width, and skewness. They observed that the measured displacement distribution remains largely non-Taylorian and were able to delineate the contributions to this non-Gaussian behavior into intrinsic dispersion and macroscopic flow heterogeneity due to sample (such as packing) heterogeneity. Their experimental results of dispersion coefficient are in quantitative agreement with both theory[16] and simulations[17] with logarithmic dependence on the Peclet number. It has been found that the flow profile at the pore level, whether it is set by a straight pipe, by the curved channels in packed spheres, or by turbulence, does not appear to have pronounced effects on dispersivity in the mechanically

mixed regime. It is possible that such sample-scale flow heterogeneity is a significant cause of confusion in earlier work.

To further expand the range of diffusion constants for investigating flow and dispersion, Granwher *et al.*[18] have applied the NMR remote detection concept to image the flow of xenon gas through porous rocks. Remote detection NMR utilizes two sets of rf coils to separate spatially the excitation and detection of magnetization. For example, the imaging encodings are applied by the excitation coil and then the magnetization is rotated to align with the static field. This magnetization and the fluid will flow continuously during the time between the excitation and the detection to the detection area. The detection coil measures the encoded magnetization by free induction decay (FID). The time between the excitation and the detection (and, thus, the travel distance) is limited by the spin-lattice relaxation of the fluid. This idea has its roots in several previous techniques such as zero-field NMR and field cycling experiments.

A natural consequence of remote detection is that the received signal is dependent on the flow pattern in the sample. Fluid from the far end of the sample will arrive later than the fluid closer to the detector, while no signal will be detected from a stagnant region that is not effectively connected to the flow field. Heterogeneity in the flow field introduces preferential flow paths as a result of the structural heterogeneity. Furthermore, this technique can be used to image the flow field in a very large porous sample.

B. Multiple diffusion NMR scattering experiment

Pulsed gradient spin-echo (PGSE)–NMR provides only a projection of the displacement profile along a single direction. Several groups have explored NMR scattering of multiple orientations, which measures the correlation of displacement along different orientations by tracking the spatial history of molecules with different combinations of gradient orientations.[19–21] For instance, Cheng and Cory showed that the two-dimensional multiple NMR scattering technique (double PGSE) can detect anisotropy in randomly oriented yeast cells,[19] and they established the theory for such techniques.

Recently, Callaghan and Komlosh[21] have used double PGSE to detect microscopical anisotropy of a polydomain lyotropic liquid crystal sample which is macroscopically isotropic material due to the random orientation of the domains. A difference between echo attenuations in the low q regime with different combinations of gradient directions can indicate microscopic anisotropy. Komlosh *et al.* demonstrated double PGSE using a phantom made of randomly oriented fused silica glass tubes and cortical gray matter from *rhesus* monkey brain. The double-PGSE experiment showed diverging echo attenuation profiles between collinear and orthogonal gradient combinations in the low q regime for both samples, revealing their microscopic anisotropy with a high signal-to-noise ratio.[22] Also, combinations of double PGSE and image acquisition have also been reported.[23] The novelty of the work from Komlosh *et al.* is that they experimentally demonstrated that the microscopic anisotropy of macroscopically isotropic sample, which is not accessible with conventional single direction PGSE method, can be detected at low q regime using double PGSE. Such techniques may be useful for studying porous media and biological tissues, such as tendons[24,25] and brain gray matter with potential clinical applications because of its sensitivity in the low q regime compatible with clinically available gradient strength.[23]

C. Diffusion kurtosis imaging (DKI)

Diffusion tensor imaging (DTI) measures diffusion coefficient in three-dimensional space and has been widely used to investigate the microstructure of biological tissues,[26] particularly for brain white matter. However, DTI is based on the assumption that the molecular diffusion follows a Gaussian displacement distribution, while, in fact, the diffusion propagator in biological tissue is often non-Gaussian. Thus, a full displacement distribution should be measured.[27,28] On the other hand, q-space imaging requires strong gradients and long imaging times and has been challenging to implement *in vivo*. Recently, Jensen *et al.* developed a method to quantify the deviation of diffusion displacement from Gaussian behavior (kurtosis) with only a modest increase of b values from those typically used in diffusion weighted imaging[29] using standard diffusion imaging sequence. In short, kurtosis is a measure of the "peakedness" of a probability distribution and, thus, provides a quantitative metric of the degree to which diffusion deviates from Gaussian behavior.[30]

Jensen *et al.* showed that a standard pulsed field gradient NMR sequence can be used to quantify diffusion kurtosis in cortical gray matter and frontal white matter with b values not exceeding 2500 s/mm^2. The kurtosis map showed markedly better gray/white matter contrast than that from the commonly used diffusion map, as demonstrated in Fig. 1. It is argued that the principal advantage of DKI over DTI is that DKI provides a specific measure of tissue structure, whereas DTI is often affected by other confounding factors such as contributions from macromolecules.

DKI requires the standard diffusion imaging sequence with straightforward postprocessing, while it reveals more information regarding tissue structure. Potential clinical applications of DKI include white matter diseases, structural changes following stroke, and lung imaging.

D. Diffusion-based composition analysis

Fluids in natural systems are often mixtures containing large number of different types of molecules. Crude oil is a good example in that it contains mostly alkane chains ranging from methane (CH_4) to those with over 100 carbon atoms. The composition of crude oil determines its properties, such as viscosity and phase diagram, which are critical in designing and optimizing crude oil production. However, commonly used analytical techniques such as high-resolution NMR spectroscopy, gas chromatography, and mass spectrometry require delicate instrumentation and are currently not suitable for field application. NMR diffusion has been shown to provide a promising method to determine composition and viscosity *in situ*.[31]

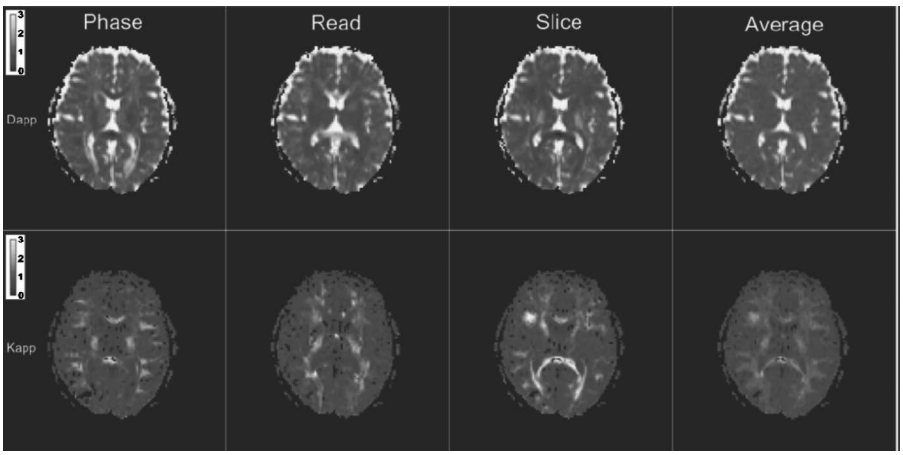

FIG. 1. Maps of the apparent diffusion constant (first row) and apparent diffusion kurtosis (second row) for human brain. The averaged kurtosis map shows better gray/white matter contrast. Magnetic Resonance in Medicine, **53**(6), 1432–1440 (2005). Copyright 2005 Wiley-Liss, Inc. Reprinted with permission of Wiley-Liss, Inc., a subsidiary of John Wiley & Sons, Inc. (Ref. 29).

It is well-known that the molecular diffusion constant (D) is dependent on molecular size.[32] In a mixture, one would expect that small molecules diffuse faster than large ones, while subject to a common fluid environment contributed from all molecules. Thus, the distribution of the composition would be reflected in the distribution of diffusion constants. In fact, Freed *et al.* have extended the understanding of diffusion in polymer melts to a broader chain length distribution of alkane mixtures and established a robust scaling relationship between diffusion constant and chain length.[31] Their model divides the diffusion coefficient of a mixture into two parts. The first part depends on the properties of the individual molecule, such as its size, shape, and stiffness, while the second part depends on the bulk fluid properties, such as the density and friction coefficients for a monomer which should be identical for all molecules within the mixture. Thus, the diffusion coefficient for the ith component (D_i) should have the form

$$D_i = N_i^{-\nu} g(\{N_i\}), \tag{1}$$

where N_i is the chain length, and $g(\{N_i\})$ is a function of all the components in the mixture and is related to the viscosity. They have shown the validity of this scaling from a large body of experimental data on alkane mixtures and found that the factor g is a function of the mean chain length only. Using this new scaling relation, a chain length distribution can be directly obtained from NMR diffusion measurements.[33]

E. Ultrafast techniques for diffusion and relaxation measurements

Diffusion measurement can be described conceptually in a general fashion as follows. The application of rf pulses and field gradients produces spatial (e.g., sinusoidal) modulation of magnetization. Diffusion between the positive and negative regimes of magnetization causes the decay of the amplitude of the modulation. With shorter wavelength of the modulation, the amplitude decay rate is higher. Thus, measurement of the modulation dependence of the decay rate can determine diffusion constant.

Most diffusion-related techniques require several separate scans with different modulations in order to complete the diffusion decay curve. However, it is possible to create a magnetization modulation that is a mixture of several sinusoidal modulations so that data for multiple modulations can be obtained in a single scan. We design a pulse sequence to create multiple echoes and encode each echo differently. Thus, a single scan of the sequence can produce multiple data points to determine, for example, diffusion.

To illustrate this, let us consider a static magnetic field gradient (g) and a train of three pulses with tipping angles α_1, α_2, and α_3, and the time spacings between them to be τ_1 and τ_2,

$$\alpha_1 - \tau_1 - \alpha_2 - \tau_2 - \alpha_3 - \text{acquisition}(\tau_3). \tag{2}$$

This sequence allows a total of five coherence pathways (Q) to be observed,

Echo number	q_0	q_1	q_2	q_3
1	0	0	0	−1
2	0	1	0	−1
3	0	−1	1	−1
4	0	0	1	−1
5	0	1	1	−1

(3)

$q_3 = -1$ for the detection period. The first coherence pathway $(0,0,0,-1)$ gives rise to a FID signal, and all others produce echoes. The second signal is, in fact, a stimulated echo, and the third one is a spin echo that has been refocused twice.[34] When the ratio of τ_1 and τ_2 is set to 1:3, all echoes are separated by τ_1.[35]

The complex magnetization for each coherence pathway can be written as a product of four factors,

$$M_Q = A_Q \cdot B_Q \cdot C_Q \cdot F_Q, \tag{4}$$

where A_Q is the frequency spectrum of the resulting signal and depends only on the rf pulses, B_Q reflects attenuation due to molecular diffusion, C_Q contains the relaxation attenuation factors, and F_Q reflects phase shifts and attenuations due to flow. The attenuation B_Q induced by unrestricted, isotropic diffusion is $B_Q = \exp(-b_Q D \gamma^2 g^2 \tau_1^3)$, for a 1:3:9 time spacing. Each echo will be associated with a unique b_Q and, thus, one scan of the sequence can be sufficient to obtain the diffusion constant.[36] In contrast to multiple encoding at different spatial slices, such multiple modulations achieve different encodings through Fourier spatial modulation of the magneti-

zation. Signals of all echoes originate from the entire excitation volume.

In contrast to the scalar diffusion constant for isotropic diffusion, anisotropic diffusion is described by a diffusion tensor with six independent coefficients. In order to measure such tensor, diffusion weightings along different directions are required. The multiple-modulation-multiple-echo (MMME) method can produce simultaneous spatial modulations along multiple directions and, thus, sensitize the signals to multiple diffusion tensor elements simultaneously.

To illustrate this method, let us first consider the three-pulse sequence with a constant z gradient during the entire sequence and only one x-gradient pulse G_{x2} during τ_2. Since only the latter three echoes exhibit transverse magnetization during τ_2, they alone are modulated by G_{x2}. In order to form the latter three echoes, another identical G_{x2} gradient pulse must be applied after the second signal to unwind the modulation. In this case, diffusion along x induces an identical amount of decay only for the latter three echoes. On the other hand, all echoes experience a different amount of decay due to diffusion along z. As a result, one scan produces four echoes with a different range of decay along x and z and, thus, allows measurement of the two-dimensional (2D) diffusion tensor. An experiment using four rf pulses to obtain the 2D diffusion tensor was reported previously.[37]

Compared to one-dimensional (1D) MMME, a tensor experiment extracts more information from the same number of echoes and, thus, the uncertainty of the result can be higher and correlated. Quantitative metrics such as the condition number have been employed for the optimization of MMME sequence.[38] Recently, Cho *et al.* have shown a further optimization of the MMME sequence to measure the full diffusion tensor in one scan.[39]

Several other modifications have been explored for rapid measurement of the flow velocity vector along arbitrary directions[40] and ultrafast imaging.[41] The work to demonstrate simultaneous measurement of T_1, T_2, and D is ongoing in the authors' laboratory. These ultrafast techniques may be useful to accelerate traditional measurements, such as DTI (Ref. 38) in clinical applications, or perhaps more importantly to monitor fast physical and chemical processes that demand high temporal resolution, such as flow of mixtures, irregular movement, and chemical reactions.

III. INTERNAL MAGNETIC FIELD

When a heterogeneous sample is placed in a magnetic field, a spatially varying field appears inside the pore space due to the magnetic susceptibility mismatch between the host solid material and the pore-filling fluid. Such internal field inhomogeneity was first recognized by Brown,[42] who computed magnetic field distributions from a single magnetized grain and a random packing of grains and who observed the effects of such distributions on the decay of NMR signals. Drain[43] studied the NMR line broadening due to field inhomogeneity in a powdered sample. Recently, Sen and Axelrod[44] reviewed the literature on internal fields and further extended the computation for a pack of cylinders. Internal field is, in general, characterized by a very wide distribution of gradients and has since been observed[45–48] through its effect upon transverse spin-spin relaxation time. Such background gradients within randomly packed microspheres can be estimated as $\Delta B/d$, where ΔB is the width of the magnetic field distribution and d is the pore size. For instance, this background gradient has been estimated to be up a few hundred G/cm at high magnetic field strengths.[48–50]

We postulated that the internal field carries a fingerprint of the internal structure of materials[14] and, therefore, pore geometry may be characterized by probing the internal field. The spatial profile of this internal magnetic field can be determined by the structure of the underlying porous medium. Such an assertion is qualitatively expected, and a quantitative connection between the pore structure and the magnetic field distribution has been demonstrated. For example, by numerically simulating the internal magnetic field from a random-dense pack of spheres,[51] it has been shown that the two-point correlation function of the internal field is closely related to the structural factor of the spheres. Experimental decay due to diffusion in the internal field (DDIF) technique is based on internal field and has shown to measure pore size distribution.[14]

A. Internal field compensation sequences

In order to accurately measure the diffusion coefficient in heterogeneous systems, suppression of background gradients is crucial. The effects of spatially constant gradients can be fully compensated by a combination of bipolar gradients and refocusing pulses.[52,53] However, internal field gradients are not spatially constant especially when the spin displacement becomes comparable to the length scale of local structures, such as pore size. For instance, Seland *et al.* showed that a diffusion measurement in a heterogeneous field is susceptible to variation of the background gradient for the case of long diffusion times.[49] Thus, a more appropriate model employs two background gradients during the encoding and decoding intervals independently to describe the variation in background gradients. Sun *et al.* and Galvosas *et al.* modified the diffusion sensitizing gradients of the conventional bipolar pulsed gradient stimulated echo (bPGSTE) sequence with a pair of asymmetric gradients according to a modulation factor. They dubbed this technique as "magic asymmetric gradient stimulated echo (MAGSTE)."[50,54–56] Because the MAGSTE sequence self-compensates the cross term between the applied and background gradients within the encoding/decoding interval, it can suppress those background gradients that vary during the evolution time but remain constant during the encoding/decoding interval. Recently, Sun further demonstrated (Fig. 2) that the surface-to-volume ratio measured from the MAGSTE diffusion sequence agreed well with a theoretical prediction for a packed glass bead systems, whereas the conventional bPGSTE method significantly underestimated the surface-to-volume ratio.[50]

B. DDIF

DDIF stands for decay due to diffusion in the internal field,[14,57] and this technique detects the diffusion of the fluid molecules in the internal field and uses that information to derive pore sizes.

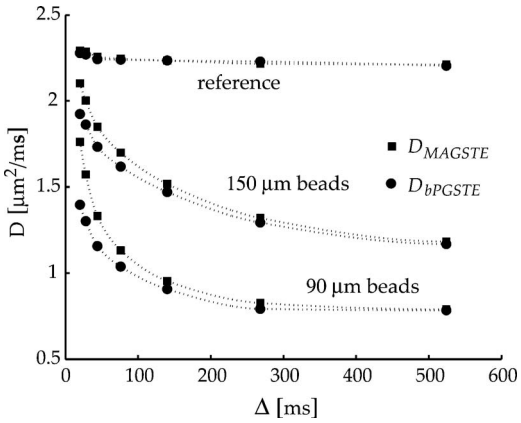

FIG. 2. The measured diffusion coefficient as a function of the evolution time using the MAGSTE and bPGSTE techniques. For the glass bead phantoms, bPGSTE measurements were significantly lower than those of MAGSTE technique, especially at short evolution intervals. Reference data are from bulk water. Reproduced from Ref. 50.

Since the internal field is the result of a superposition of fields from all grains, it naturally reflects the spatial arrangement of such grains. For example, the internal field varies over the length scale of the pore size. Hence, the internal field is generally very different on opposite sides of a pore, while there is no rapidly oscillating field within a pore.[57] Audoly *et al.* has shown[51] that the correlation function of the internal field is closely related to the pore size and structure factor. A DDIF experiment first establishes a spin magnetization modulation that mimics the spatial variation of the internal magnetic field. As a result, the magnetization at the opposite sides of a pore will be, in general, opposite in sign. Then, molecular diffusion of the fluid results in decay of the magnetization profile when the diffusion distance is comparable to the pore size. Measurement of such time-dependent evolution determines the decay time constant τ and, therefore, the pore diameter $d=\pi\sqrt{D\tau}$.

Experimentally, the magnetization is first rotated to the transverse plane to precess in the internal field for a period of t_e. Then, it is rotated back to the longitudinal direction to allow diffusion to occur. After this diffusion time of T_d, the magnetization is rotated to transverse plane for detection as a stimulated echo. The T_d decay of the echo is measured and the decay rate $(1/\tau)$ is used to calculate the pore size. Since the range of T_d is from microsecond to several T_1 (often several seconds for water), the pore sizes to be detected by DDIF is from submicrons to several hundred microns using water. Since the magnetization during T_d is in longitudinal plane, the decay process is not due to T_2.

C. DDIF applications

The pore space of sedimentary rocks is, in general, composed of large pores (pore bodies) connected with other pore bodies via relatively smaller pore throats. In addition, pores often have a distribution of sizes. As a result, the DDIF decay exhibits multiexponential behavior as a result of the pore size distribution. Below, several applications of DDIF are listed with a brief description.

Pore sizes and pore body-to-throat ratio. It is known that many rocks exhibit a pore size distribution dominated by one peak that is often interpreted as the main pore body. However, other rocks exhibit very broad pore size distributions reflecting the heterogeneity of the materials. The DDIF technique has been applied to study sandstone and carbonate rocks,[14,58–61] and the DDIF-obtained pore sizes are in good agreement with the microscopy-derived pore sizes.

A simple overlay of DDIF data and mercury porosimetry immediately identifies pore bodies and throats, thus obtaining a model of the pore space. Such a comparison showed that in Berea sandstone, the pore space consists of large cavities of about 85 μm connected via 15 μm channels or throats.[60]

Pore shape. A recent study[61] used a combination of DDIF and mercury intrusion porosimetry to obtain both pore body linear size and pore body volume. In addition, a simple analysis of two-dimensional thin-section images provides a characterization of pore shape from only geometric properties. The authors concluded that for Berea sandstone, the pore bodies are mostly much elongated tubelike structures with a cross-sectional size of 85 μm and a length spanning several grains.

Carbonate rocks. Carbonate rocks often contain pores of various sizes ranging from submicrons to millimeters. In the case where the large pores and small pores are spatially close by, water molecules that travel between pores in less than T_2 will result in a single peak in a T_2 distribution. Thus, T_2 may not be capable of differentiating pore sizes. On the other hand, DDIF is not susceptible to such a limitation and, in fact, it identified three populations of pores in a carbonate sample.[14] In addition, DDIF has also been applied to study a series of carbonate rocks and examined the evolution of the pore geometry in diagenesis.[59,60]

Drainage and imbibition. Two-phase flow has been studied by combination of magnetic resonance imaging (MRI) and DDIF techniques.[62] The water movement in the sample was first monitored by MRI. However, the limited MRI resolution does not address the water saturation at a pore scale. DDIF data showed the drastically different pore-filling patterns under different saturation processes.

Cell membrane permeability. In a blood sample, red blood cells (RBC) exhibit a slightly different magnetic susceptibility from that of water; thus, the magnetic field varies between the inside and the outside of the RBC. DDIF experiments were used to create a magnetization difference across the membrane, and water transport through the membrane was measured.[63] It potentially allows quantification of membrane permeability of cells and tissues in clinic.

Trabecular bone structure. Trabecular bones exhibit a complex internal structure that is an important contributor to bone strength. Recent MRI efforts have focused on high-resolution three-dimensional imaging. However, it is difficult to attain a drastic improvement in resolution beyond the current levels (100 μm) in clinical implementation, primarily due to clinically allowed MRI scan times.

Sigmund *et al.*[64] presented a novel approach using DDIF to obtain statistical properties of the trabecular structure without high-resolution MRI. *In vitro* DDIF data on bovine trabecular bone samples show a clear correlation with the

measured surface-to-volume ratio (S/V), demonstrating DDIF's sensitivity to bone structure. DDIF has the potential for clinical application in osteoporosis diagnosis and drug development.

IV. 2D NMR OF RELAXATION AND DIFFUSION

One-dimensional relaxation measurements are widely used, such as the Carr-Purcell-Meiboom-Gill[65,66] (CPMG) method to measure magnetization decay due to T_2 and then to obtain a T_2 distribution through Laplace inversion. This is similar to the conventional 1D Fourier spectroscopy. Similar to two-dimensional Fourier spectroscopy, 2D NMR of relaxation and diffusion can be performed, in general, to obtain data as a 2D matrix with two independent variables. Such data will be processed by 2D Laplace inversion to obtain the 2D spectrum of relaxation and diffusion.[67] The benefit of the 2D NMR is the enhanced resolution compared to the corresponding 1D experiments. For example, for a sample with broad distribution of T_1 and T_2, a T_1-T_2 correlation spectrum can better determine the T_1/T_2 ratio of the species than separate T_1 and T_2 experiments.

A two-dimensional experiment and its pulse sequence can, in general, be separated into two parts, and the spin dynamics are governed by two different processes or Hamiltonians. For example, the T_1-T_2 correlation experiment[10,67] can be performed using an inversion recovery sequence as the first part and a CPMG as the second part,

$$\underbrace{\pi-\tau_1}_{\text{first part}}-\underbrace{\frac{\pi}{2}-t_e/2-[\pi-t_e]_N}_{\text{second part}}, \tag{5}$$

where N is the echo number. The first time variable is τ_1 and the second one is $\tau_2=Nt_e$. The signal equation is then

$$M(\tau_1,\tau_2)=\int\int e^{(-\tau_1/T_1-\tau_2/T_2)}\mathcal{F}(T_1,T_2)dT_1dT_2, \tag{6}$$

where M is the magnetization deviation from equilibrium and $\mathcal{F}(T_1,T_2)$ is the probability density of molecules with specific T_1 and T_2. To obtain $\mathcal{F}$ from the measured M, a 2D Laplace inversion is needed (see Sec. VI for more discussion).

Diffusion can also be included to form a 2D sequence, such as the $D-T_2$ experiment to obtain a correlated distribution of the diffusion coefficient D and T_2.[67] Such experiments have been used to distinguish water and oil in a mixture.[13] In addition, the $D-T_2$ map can also be used to detect restricted diffusion in porous media.[7,68] A few areas of applications are listed below.

Early 2D NMR of relaxation. Two-dimensional measurements of spin relaxation were proposed in early 1980s (Ref. 12) to study heterogeneous mixtures. English *et al.* reported[11] experimental and numerical techniques for obtaining the 2D correlation spectrum of T_1-T_2. However, the Laplace inversion algorithm used was performed on supercomputers due to the slow speed and the requirement of a large amount of computer memory. The new inversion algorithm [fast Laplase inversion (FLI)] (Ref. 10) significantly reduced the computer memory and speed requirement and can be used on regular personal computers (see Sec. VI for more discussion).

Well logging. Since 2002, 2D NMR sequences such as $D-T_2$ and T_1-T_2 correlation have been used in the Schlumberger NMR well-logging systems.[69] The diffusion constants of water and oil are often significantly different (often a factor of 10 or more) so that the signals of oil and water are easily identified on a $D-T_2$ map. This ability to distinguish oil and water is important to many well-logging interpretations, including measurements of oil saturation, oil viscosity, bound water, and permeability. In addition, measurements at different depths in the formation also provide important information about invasion and native fluid composition. Three-dimensional measurements of $D-T_1-T_2$ have also been performed in well logging to assist in the characterization of oil, water, and gases in rocks.

Food stuff. Food products are generally a mixture of many components. For example, milk, cream, and cheeses are primarily a mixture of water, fat globules, and macromolecules. The new 2D experiments of relaxation and diffusion[70] appear to offer a new method to identify and quantify the components in dairy products. The two components are well separated in the 2D maps, while they may heavily overlap in 1D spectra. We find that some microscopic properties of the products can be reflected in the relaxation and diffusion properties. Such new techniques ($D-T_2$, $D-T_1-T_2$, etc.) are likely to be useful to assist in characterization of the products for quality control and quality assurance by, e.g., quantification of liquid fat content.

Application in cements. 2D NMR correlation experiments (T_1-T_2 and T_2-T_2) have been performed on hydrating cement pastes.[71,72] A cross peak in the two-dimensional relaxation spectrum was observed and was interpreted as evidence of exchange of water between gel and capillary pores. The exchange rate was found to be on the order of 5 ms^{-1}. A water diffusion coefficient inferred from the exchange rate and the cement particle size was found to compare favorably with the results of molecular dynamics simulations. The dynamics of water in the nanoscale environment is very important in understanding the nanopore structure and the hydration reactions during the evolution of the calcium silicate hydrate gel in cement.

Chemical exchange experiments. 2D NMR (T_2-T_2 or ARTDECO) was demonstrated in 1993 (Ref. 73) to detect chemical exchange between water and urea protons in solution. A cross peak was observed, and the mixing time dependence of the intensity of this cross peak was used to derive the exchange time. Callaghan and co-workers have used 2D NMR to study diverse subjects in physics and chemistry, such as anisotropic water diffusion in liquid crystals,[74] dextran exchange in multilayer capsules, and water transport between pores.[75]

V. MRI OF ROCKS: HETEROGENEITY

MRI provides a unique opportunity to study porous media on many length scales. Macroscopic information, typically over millimeters and longer length, can be directly inferred from the MRI images. Microscopic information can be

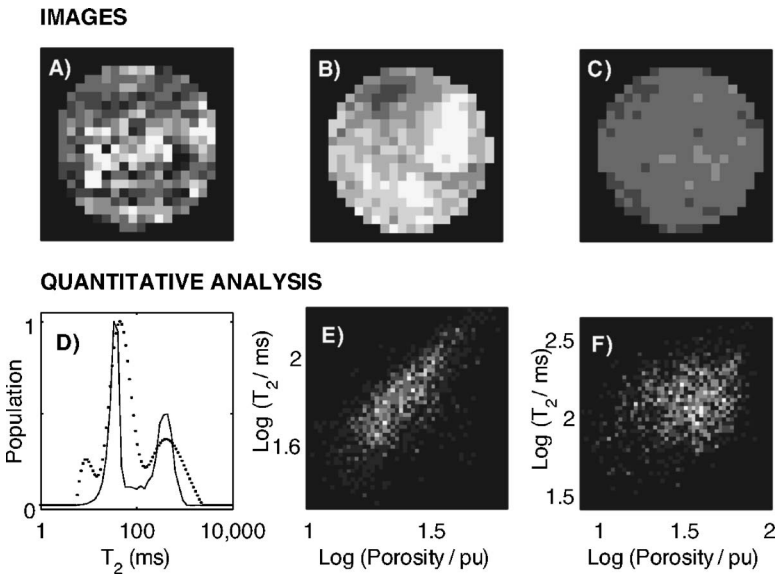

FIG. 3. MRI of rocks and quantitative analysis (Ref. 86). [(A)–(C)] 2D slices of the porosity images of three carbonate cores, cores are 2 cm diameter, measured with 1 mm resolution; the porosity gray scale goes up to 40 p.u. (D) T_2 distributions from MRI (solid line) and Laplace inversion (dotted line). [(E) and (F)] Porosity versus relaxation time correlation plots for two additional carbonates. p.u. stands for porosity unit and a pure water voxel is 100 p.u. Images were obtained by slice-selective multiple spin echo method.

obtained from spin relaxation, diffusion, and internal field properties. By measuring the variation of NMR parameters (porosity, relaxation, diffusion, etc.) over different physical locations within the sample, MRI can provide a description of spatial heterogeneity.[76–86] Additionally, the spatial correlation of these parameters may provide a new means of assessing structure and heterogeneity.

The importance of different length scales of heterogeneity is especially interesting in the characterization of reservoir rocks and can be addressed directly with MRI (Ref. 86), as shown in Figs. 3(a)–3(c). For example, Fig. 3(b) shows a sample where adjacent voxels have similar porosities, while distant voxels have widely varying porosities, indicating heterogeneity at long length scales but not at short length scales. On the other hand, Fig. 3(a) shows a sample where even adjacent voxels have widely varying porosities, indicating heterogeneity at length scales comparable to the voxel size. Finally, Fig. 3(c) shows an example of a rock that is mostly homogeneous on length scales above 1 mm. On length scales below the size of a voxel, heterogeneity can be described by the relaxation; i.e., the relaxation time distribution reflects the distribution of pore sizes. Comparison of relaxation distributions for different voxel sizes allows insight into the length scale of pore size variation. These comparisons are our attempt at *quantitative* analysis of MRI images in order to characterize the heterogeneity of porous media.

A. Spatial heterogeneity

Slice-selective multiple spin echo imaging can determine the spatial variation of porosity and T_2 relaxation time.[86] The relaxation decay in each individual voxel is typically not exponential; thus, a double exponential function is used. The T_2 from each voxel is combined to form a MRI-based T_2 distribution and compared to Laplace inversion of the CPMG signal from whole samples. It is important to note that functions such as a double exponential or stretched exponential[76,77,80,85,86] may not describe the full T_2 distribution, but they do represent some average properties of the T_2 distribution such as the mean T_2 and the width.[86] The analysis has shown that the MRI-based T_2 distribution agrees quite well with the Laplace inversion result[86] [Fig. 3(d)], both showing two major peaks with consistent amplitudes. In fact, all three samples (a–c) show similar T_2 distributions with two peaks and all agree with the corresponding Laplace inversion results. The slight difference between the T_2 distributions from the two methods, e.g., the width for each peak, is due to the spatial averaging within voxels for the double exponential fitting.

The spatial variation of the relaxation rate distribution can help us further establish the length scales over which T_2 (reflecting pore size) varies. For example, one scenario may be that each individual voxel exhibits single T_2 at either one of the two peaks. This means that within one voxel of 1 mm, the pore size is uniform and the heterogeneity of pore sizes is over a distance longer than 1 mm. However, Pomerantz *et al.* showed[86] that almost all of the voxels exhibit two relaxation rates that correspond to the two peaks. This observation indicates that the heterogeneity (T_2 and pore size) occurs well within every 1 mm voxel for these carbonate samples.

B. Spatial correlation

The spatial correlation between porosity and T_2 (both measured with this same multiple spin echo sequence) can also be investigated. Figures 3(e) and 3(f) show this correlation for two additional carbonate samples. These correlation plots are used to determine whether or not spatial regions with large porosity also have large pores (i.e., long relaxation times). If regions with large pores also have large porosity, the correlation plot will have maximum density along a straight line with a positive slope; if regions with large pores have low porosity, the correlation plot will have maximum density along a straight line with a negative slope; if there is no relationship between pore size and porosity, the correlation plot will appear circular.[87]

There is no general reason to expect any correlation between pore size and porosity for a random porous space. Surprisingly, some samples [Fig. 3(e)] show a clear relationship between pore size and porosity, while others do not [Fig.

3(f)]. This pore size–porosity correlation could arise from geological and geochemical processes during sedimentation and diagenesis, and its implications about the structure of the rock are currently being investigated.

VI. LAPLACE INVERSION

Spin relaxation and diffusion are typically manifested as decaying signals. Data analysis then often involves a Laplace inversion to obtain a spectrum (or distribution) of relaxation times or diffusion constants. The inversion is ill conditioned in the sense that small noise in the data can cause large changes in the spectrum. For experimental data with noise, the ill-conditioned nature also manifests itself as the existence of infinite number of solutions that satisfy the noise model.

One common method to handle the problem is to select a subset of the solutions, for example, the smooth solutions, and then look for the best solution within this subset. Commonly used methods include Tikonov regularization[88] and the maximum entropy method[89] to handle this and other types of inversion.[90] Several NMR papers[91–93] use regularization and they are a good introduction to this problem.

A. Resolution

One of the critical issues regarding such algorithms is the resolution of the resulting spectra. For example, given a spectrum with a single peak, one may ask the question whether the spectral width is determined by the finite signal-to-noise ratio or whether it reflects the true width of the underlying phenomenon? A second related question is how far apart must two spectral peaks be in order to be resolved as two independent contributions in the reconstructed spectrum? A recent report[94] provides a simple numerical method to estimate the resolution of such a spectrum. This method uses singular value decomposition to find the minimum singular value corresponding to the finest resolution allowed by the experimental parameters and noise. An experimentalist can use this theory to optimize the design of diffusion and relaxation experiments. This method is certainly applicable to data analysis beyond NMR.

B. Error analysis

Since Laplace inversion algorithms often use a nonlinear fitting procedure, it is difficult to ascertain the error of the resulting spectrum and other integral quantities. For example, since the conventional regularized solutions explore only a fraction of the available solution space, the estimated error based on a regularized solution may not be appropriate. Recent articles[95,96] describe a new method to estimate the error of the integrals of the relaxation spectrum without the limitation of a regularized solution.

C. Fast Laplace inversion: 2D Laplace inversion

The 2D Laplace inversion, such as Eq. (6), can be cast into the 1D form. However, the size of the kernel matrix will be huge and it is difficult to solve on current desktop computers. Thus, the 1D algorithm cannot be used directly.

It was realized[97] that many kernel functions can be separated into two factors, $k(\tau_1,\tau_2,T_1,T_2)=k_1(\tau_1,T_1)k_2(\tau_2,T_2)$. Then, Eq. (6) can be rewritten in a matrix form

$$M = K_1 F K_2' + E, \tag{7}$$

where matrices K_1, K_2, and F are discretized versions of k_1, k_2, and $\mathcal{F}$, respectively. The major benefit of the tensor product structure of the kernels is that singular value decompositions (SVDs) of K_1 and K_2 are quite manageable on desktop computers. Once the SVDs of K_1 and K_2 are obtained, the SVD of the product matrix can be evaluated quickly. Then, a method adapted from the Butler-Reed-Dawson algorithm[98] was used to find the optimal solution with regularization. The details of this algorithm (FLI) and its applications have been presented in Refs. 10, 67, and 97.

VII. INSTRUMENTATION

Porous media have been studied in the laboratory for many years using conventional NMR magnets, spectrometers, and field cycling spectrometers. However, for applications on such as rock, hydrocarbon, cements and building materials, plants, fresco, and food stuff, the samples are often large and cannot fit in a conventional NMR magnet. Hence, the NMR systems have been engineered to have the magnet inside the instrument and sample on the outside.

A. NMR well-logging tools

One of the first nuclear magnetic logging tools was developed in 1958 by Brown[99] based on Earth's field NMR. These systems have an excitation probe and a set of receive coils. One of the major disadvantages with this system is the low signal-to-noise ratio and long recovery times. Jackson *et al.*[100] used two electromagnets with their north poles facing each other to generate a remotely toroidal region. This type of design is currently used in the logging-while-drilling tools by BakerHughes[101] and operates with a proton resonance frequency in the range of 400–600 kHz. NUMAR developed and commercialized (1991) an NMR well-logging tool based on a permanent dipole magnet with a cylindrical region of sensitivity.[102] Improvement was later made to increase the signal-to-noise ratio and pulse at multiple resonance frequencies obtaining different depth "shells."[103]

In the early 1990s, Kleinberg *et al.* at Schlumberger developed a NMR logging tool with permanent magnets (2 MHz) producing a saddle point field with a sweet spot of 1.5 in. from the tool surface.[104] The rf coil was a half-coaxial cable made from copper and utilized ferrite loading to increase inductance. The second generation Schlumberger NMR well-logging tool is based on a single dipolar magnet and is able to provide four different resonance regions (shells) up to a distance of 4 in. away from the surface of the instrument. These shells are accessed by switching resonance frequencies (from 0.5 to 2 MHz) taking advantage of the decreasing field strength away from the tool. Diffusion, T_1, and T_2 data can be acquired simultaneously during continuous logging.

B. NMR MOUSE and other non-well-logging systems

One of the early developers of one sided access or unilateral magnet systems outside of the oil industry was the group led by Blumich in Aachen, Germany. Starting with a basic U-shaped magnet, they developed the NMR-MOUSE,[15] a portable NMR device for use on large objects. This original system had a rf coil situated in the magnet gap and had an investigation depth of approximately 10 mm. Diffusion measurements[105,106] and three-dimensional MRI have been achieved on modified NMR-MOUSE systems,[107] where they covered a 10 mm depth range [40 mm field of view (FOV)] using frequencies from 7.35 to 8.35 MHz. The entire apparatus was 30×30 cm^2.[107] Recently, profile NMR-MOUSE has been developed with a thin, flat sensitive volume that is suited for measuring depth profiles with a spatial resolution of 5 μm.[108] The scanner can move relative to the sample in order to obtain the different investigation depths and is able to cover a 500 μm FOV with 5 min acquisition time.

In 2006, Manz *et al.*[109] developed a portable magnet system for surface applications (called NMR-mobile lateral explorer, NMR-MOLE) that is based on the barrel magnet, but looks more similar to a Halbach circular array. The difference being that the magnets were polarized along the long axis of the magnets. The entire assembled probe was 200 mm in diameter with a homogeneous region contained in a sphere of 20 mm (subject to rf). The rf coil was a figure of eight coil designed to create rf field parallel to the surface and was tuned to the proton resonance frequency of 3.27 MHz. The system was tested on mixed cement with differing ratios of water and cement over long periods of time.[109]

The gradient at right angles to the field[110] (GARField) magnet designed by McDonald *et al.* is characterized by a B_0 field of constant magnitude in a plane parallel to the surface of the magnet and a gradient perpendicular to the face of the magnet to provide spatial resolution. However, the magnet must be moved relative to the sample through the use of a stepper motor to achieve depth determination. They were able to profile large samples (study involved cement hydration and porosity development) to a depth of 35–40 mm by moving the magnet.[110] At a distance of 50 mm (gradient of 2.9 T/m) from the magnet surface, the plane of constant resonance frequency extends over a 130×100 mm^2 area with a proton resonance frequency of 3.2 MHz.

More complex design of magnets, including novel shim poles and magnet arrays, have been reported recently, such as of Marble *et al.*,[111] Prado *et al.*,[112] Hunter *et al.*,[113] Chang *et al.*,[114] and Rahmatallah *et al.*[115] There are a wide variety of designs available with many being tailored to fulfill specific applications.

ACKNOWLEDGMENTS

The authors thank many colleagues and friends at SDR and other institutions for their immense contributions to much of the work reviewed here: L. Venkataramanan, M. Prange, R. Parker on mathematics, S. Byrnes, P. Chen, D. Freed, L. Zielinski, S. Ryu, P. N. Sen on theory and physics, N. V. Lisitza, E. E. Sigmund, X.-H. Ren, M. D. Hürlimann on NMR, C. Straley, D. F. Allen, W. Kenyon and A. Boyd on rocks and petrophysics, Q. Chen on mercury experiments, W. S. Warren, T. Brown and E. X. Guo on biomedical applications, and A. Pines, J. Granwehr, and other Pinenuts on remote detection NMR.

APPENDIX A: THEORY OF DIFFUSION EIGENMODES

This section will review the physics of diffusion in restricted geometry based on the original work of Brownstein and Tarr,[116] with an emphasis on the properties of the higher eigenmodes. Eigenmode and propagator formalisms are mathematically equivalent solutions of the diffusion equation. In fact, the diffusion propagator can be written as a sum of eigenmodes. For problems when many eigenmodes are involved, it might be convenient to use the propagator formalism. On the other hand, if only a few eigenmodes are excited in a certain experiment, such as DDIF, the eigenmode method can be advantageous. In addition, the eigenmode method allows a direct interpretation of the magnetization dynamics in terms of the underlying pore geometry.

The differential equation governing diffusion of the longitudinal nuclear spin magnetization is the well-known Torrey-Bloch equation,[117]

$$\frac{\partial}{\partial t}m(\mathbf{r},t) = D\nabla^2 m(\mathbf{r},t) - \mu m(\mathbf{r},t), \tag{A1}$$

where D is the bulk diffusion constant and μ is the bulk spin relaxation rate. m is the magnetization deviation from its equilibrium. The detected signal is $M(t)=\int m(\mathbf{r},t)dv$. A solution can be found in the general form

$$m(\mathbf{r},t) = \sum_{n=0}^{\infty} a_n \phi_n(\mathbf{r}) e^{-t/T_n}, \tag{A2}$$

where ϕ_n and T_n are eigenfunctions and eigenvalues. The eigenfunctions are normalized, $(1/V)\int dv\, \phi_n^2 = 1$, where V is the pore volume. We will set $V=1$ for simplicity. The eigenvalues are determined by the eigenequation,

$$\phi_n/T_n = -D\nabla^2\phi_n(\mathbf{r}), \tag{A3}$$

and the boundary condition at the pore surface,

$$D\hat{n}\cdot\nabla\phi_n + \rho\phi_n = 0, \tag{A4}$$

where $\hat{n}$ is the unit vector normal to surface and ρ is the surface relaxivity. From the orthogonality of the eigenmodes, one can derive that the amplitude of each mode can be determined by the initial magnetization, $m(r,0)$,

$$a_n = \int m(\mathbf{r},0)\phi_n(\mathbf{r})dv. \tag{A5}$$

This general formalism translates the complexity of the time-domain diffusion into the complexity of the eigenmodes, a stationary property determined solely by the boundary.

The spatial characteristics of the eigenmodes can be used to group the modes into two categories. One is the relaxation mode with an approximately uniform amplitude throughout the pore space. Only the lowest eigenmode ϕ_0 belongs to this

category. The second group is the diffusion mode who amplitude integrates to zero. All modes except the lowest one is in this category. Such unique spatial characteristic can be derived by considering the orthogonality of the eigenfunctions,

$$\int \phi_n \phi_m = \delta_{n,m}. \tag{A6}$$

Choose $m=0$ and note $\phi_0 \approx 1$, thus,

$$\int \phi_n \approx \delta_{n,0}. \tag{A7}$$

These two categories of modes distinquish themselves also in their decay mechanism. For the relaxation mode, the only means for the reduction of the amplitude is through spin relaxation at the surface. Hence the name relaxation mode. On the contrary, the amplitude of the diffusion modes decays by diffusing the molecules from the positive-amplitude regions to the negative-amplitude regions. The decay rate of the diffusion modes is much less sensitive to surface relaxation. Some of the diffusion modes can be sensitive to pore-to-pore connectivity.[118]

Brownstein and Tarr showed[116] elegantly that for an arbitrary geometry under the fast diffusion condition, the lowest eigenmode ϕ_0 is a constant in space, and ϕ_0 dominates the simple relaxation experiments and, thus, produces a single exponential decay. In contrast, DDIF creates nonuniform magnetization and, thus, detects other diffusion modes.

APPENDIX B: 2D NMR OF DIFFUSION SYSTEMS

Consider a T_1-T_2 experiment as shown below,

$$\pi - \tau_1 - \frac{\pi}{2} - t_e/2 - [\pi - t_e]_N. \tag{B1}$$

The first 180° pulse inverts the nuclear magnetization which then experiences T_1 relaxation. After a period of time τ_1, a CPMG pulse sequence is applied to rotate the magnetization from the axis along the external field to the transverse plane and to record the transverse relaxation process, T_2. Since both T_1 and T_2 dynamics are involved in this experiment, we need to consider two sets of eigenmodes corresponding to the T_1 and T_2 dynamics. The main differences between the two sets of modes are the bulk relaxations (T_{1b} and T_{2b}) and surface relaxivities (ρ_1 and ρ_2). We call the two sets of modes as L modes and T modes and denote them as ϕ_n^L and ϕ_n^T, respectively.

During the τ_1 period, the magnetization dynamics is described by L modes. The magnetization at the end of the τ_1 period is

$$m1(\mathbf{r},\tau_1) = \sum_{i=0}^{\infty} a_i \phi_i^L(\mathbf{r}) e^{-\tau_1/T_{1i}}. \tag{B2}$$

Here, a_n is determined by the initial magnetization after the π pulse, $m_0(\mathbf{r})=1$. After the $\pi/2$ pulse, the magnetization is rotated to the transverse plane so that the spin dynamics is governed by T modes. Thus, the evolution of the CPMG echo signal is

$$m(\mathbf{r},\tau_1,\tau_2) = \sum_{j=0}^{\infty} b_j \phi_j^T(\mathbf{r}) e^{-\tau_2/T_{2j}}, \tag{B3}$$

where b_j is determined by $m(\mathbf{r},\tau_1)$,

$$b_j = \int m1(\mathbf{r},\tau_1)\phi_j^T(\mathbf{r})dv. \tag{B4}$$

The detected time-domain signal is simply an integral of magnetization,

$$S(\tau_1,\tau_2) = \int dv \cdot m(\mathbf{r},\tau_1,\tau_2), \tag{B5}$$

$$= \sum_{i,j} s_{ij} e^{-\tau_1/T_{1i}-\tau_2/T_{2j}}, \tag{B6}$$

where $s_{ij}=\langle \phi_j^T | 1\rangle\langle \phi_j^T | \phi_i^L\rangle\langle \phi_i^L | 1\rangle$ and it is, in fact, the 2D spectrum. Here, we used the quantum mechanical notation $\langle \phi | \psi\rangle = \int dv \cdot \phi\psi$. One of the important features of s_{ij} is that it measures the overlap integral of different eigenmodes (T and L modes). For example, if the T and L modes are identical, there will be no cross peaks.

[1] S. D. Senturia and J. D. Robinson, SPE J. **10**, 237 (1970).
[2] M. H. Cohen and K. S. Mendelson, J. Appl. Phys. **53**, 1127 (1982).
[3] P. G. de Gennes, C. R. Acad. Sci. III **295**, 1061 (1982).
[4] R. Kleinberg, *Encyclopedia of Nuclear Magnetic Resonance*, edited by D. M. Grant and R. K. Harris (Wiley, New York, 1995).
[5] W. P. Halperin, F. D'Orazio, S. Bhattacharja, and J. C. Tarczon, *Molecular Dynamics in Restricted Geometries*, edited by J. Klafter and J. Drake (Wiley, New York, 1989).
[6] D. E. Woessner, J. Phys. Chem. **67**, 1365 (1963).
[7] P. P. Mitra, P. N. Sen, L. M. Schwartz, and P. Le Doussal, Phys. Rev. Lett. **68**, 3555 (1992).
[8] D. G. Cory and A. N. Garroway, Magn. Reson. Med. **14**, 435 (1990).
[9] P. T. Callaghan, A. Coy, D. MacGowan, K. J. Packer, and F. O. Zelaya, Nature (London) **351**, 467 (1991).
[10] Y.-Q. Song, L. Venkataramanan, M. D. Hürlimann, M. Flaum, P. Frulla, and C. Straley, J. Magn. Reson. **154**, 261 (2002).
[11] A. E. English, K. P. Whittall, M. L. G. Joy, and R. M. Henkelman, Magn. Reson. Med. **22**, 425 (1991).
[12] H. Peemoeller, R. K. Shenoy, and M. M. Pintar, J. Magn. Reson. **45**, 193 (1981).
[13] M. D. Hürlimann, L. Venkataramanan, and C. Flaum, J. Chem. Phys. **117**, 10223 (2002).
[14] Y.-Q. Song, S. Ryu, and P. N. Sen, Nature (London) **406**, 178 (2000).
[15] G. Eidmann, R. Savelsberg, P. Blümler, and B. Blümich, J. Magn. Reson., Ser. A **122**, 104 (1996).
[16] P. G. Saffman, J. Fluid Mech. **7**, 194 (1960).
[17] R. Maier, Phys. Fluids **12**, 2065 (2000).
[18] J. Granwehr, E. Harel, S. Han, S. Garcia, A. Pines, P. N. Sen, and Y.-Q. Song, Phys. Rev. Lett. **95**, 075503 (2005).
[19] Y. Cheng and D. G. Cory, J. Am. Chem. Soc. **121**, 7935 (1999).
[20] S.-I. Han, S. Stapf, and B. Blümich, J. Magn. Reson. **146**, 169 (2000).
[21] P. T. Callaghan and M. E. Komlosh, Magn. Reson. Chem. **40**, S15 (2002).
[22] M. E. Komlosh, F. Horkay, R. Z. Freidlin, U. Nevo, Y. Assaf, and P. J. Basser, J. Magn. Reson. **189**, 38 (2007).
[23] M. E. Komlosh, M. J. Lizak, F. Horkay, R. Z. Freidlin, and P. J. Basser, Proceedings of the 47th ENC, Asilomar, California, 23–28, 2006 (unpublished).
[24] J. Wellen, K. G. Helmer, P. Grigg, and C. H. Sotak, J. Magn. Reson. **170**, 49 (2004).
[25] R. Fechete, D. Demco, U. Eliav, B. Blümich, and G. Navon, NMR Biomed. **18**, 577 (2005).
[26] P. J. Basser, J. Mattiello, and D. LeBihan, Biophys. J. **66**, 259 (1994).
[27] T. Neindorf, D. G. Norris, and D. Leibfritz, Magn. Reson. Med. **32**, 672 (1994).
[28] M. D. King, J. Houseman, S. A. Roussel, N. van Bruggen, S. Williams,

and D. Gadian, Magn. Reson. Med. **32**, 707 (1994).
[29] J. H. Jensen, J. A. Helpern, A. Ramani, H. Lu, and K. Kaczynski, Magn. Reson. Med. **53**, 1432 (2005).
[30] K. P. Balanda and H. L. MacGillivray, Am. Stat. **42**, 111 (1988).
[31] D. Freed, L. Burcaw, and Y.-Q. Song, Phys. Rev. Lett. **94**, 067602 (2005).
[32] A. Einstein, Ann. Phys. **17**, 549 (1905).
[33] D. Freed, J. Chem. Phys. **126**, 174502 (2007).
[34] Y.-Q. Song, J. Magn. Reson. **157**, 82 (2002).
[35] J. Hennig, Concepts Magn. Reson. **3**, 179 (1991).
[36] Y.-Q. Song and X. Tang, J. Magn. Reson. **170**, 136 (2004).
[37] X.-P. Tang, E. E. Sigmund, and Y.-Q. Song, J. Am. Chem. Soc. **126**, 16336 (2004).
[38] E. E. Sigmund and Y.-Q. Song, Magn. Reson. Imaging **24**, 7 (2006).
[39] H. Cho, X.-H. Ren, E. E. Sigmund, and Y.-Q. Song, J. Chem. Phys. **126**, 1 (2007).
[40] H. Cho, X.-H. Ren, E. E. Sigmund, and Y.-Q. Song, J. Magn. Reson. **186**, 11 (2007).
[41] H. Cho, L. Chavez, E. E. Sigmund, D. P. Madio, and Y.-Q. Song, J. Magn. Reson. **179**, 267 (2006).
[42] R. J. S. Brown, Phys. Rev. **121**, 1379 (1961).
[43] L. E. Drain, Proc. Phys. Soc. London **80**, 1380 (1962).
[44] P. N. Sen and S. Axelrod, J. Appl. Phys. **86**, 4548 (1999).
[45] R. J. S. Brown and P. Fantazzini, Phys. Rev. B **47**, 14823 (1993).
[46] R. M. Weisskoff, C. S. Zuo, J. L. Boxerman, and B. R. Rosen, Magn. Reson. Med. **31**, 601 (1994).
[47] G. C. Borgia, R. J. S. Brown, and P. Fantazzini, Phys. Rev. E **51**, 2104 (1995).
[48] M. D. Hürlimann, J. Magn. Reson. **131**, 232 (1998).
[49] J. G. Seland, G. H. Sorland, K. Zick, and B. Hafskjold, J. Magn. Reson. **146**, 9 (2000).
[50] P. Z. Sun, J. Magn. Reson. **187**, 177 (2007).
[51] B. Audoly, P. N. Sen, S. Ryu, and Y.-Q. Song, J. Magn. Reson. **164**, 154 (2003).
[52] L. L. Latour, L. Li, and C. H. Sotak, J. Magn. Reson., Ser. B **101**, 72 (1993).
[53] R. M. Cotts, T. Sun, J. Marker, and M. J. R. Hoch, J. Magn. Reson. **83**, 252 (1989).
[54] P. Z. Sun, J. G. Seland, and D. G. Cory, J. Magn. Reson. **161**, 168 (2003).
[55] P. Z. Sun, S. A. Smith, and J. Zhou, J. Magn. Reson. **171**, 324 (2004).
[56] P. Galvosas, F. Stallmach, and J. Karger, J. Magn. Reson. **166**, 164 (2004).
[57] Y.-Q. Song, Concepts Magn. Reson. **18A**, 97 (2003).
[58] Y.-Q. Song, Magn. Reson. Imaging **19**, 417 (2001).
[59] W. E. Kenyon, D. F. Allen, N. V. Lisitza, and Y.-Q. Song, Proceedings of the SPWLA 43rd Annual Meeting, 2002, Paper No. III.
[60] Y.-Q. Song, N. V. Lisitza, D. F. Allen, and W. E. Kenyon, Petrophysics **43**, 420 (2002).
[61] Q. Chen and Y.-Q. Song, J. Chem. Phys. **116**, 8247 (2002).
[62] Q. Chen, M. Gingras, and B. Balcom, J. Chem. Phys. **119**, 479 (2003).
[63] N. V. Lisitza, W. S. Warren, and Y.-Q. Song, J. Magn. Reson. **187**, 146 (2007).
[64] E. E. Sigmund, H. Cho, P. Chen, S. Byrnes, Y.-Q. Song, E. X. Guo, and T. Brown, Magn. Reson. Med. **59**, 28 (2008).
[65] H. Y. Carr and E. M. Purcell, Phys. Rev. **94**, 630 (1954).
[66] S. Meiboom and D. Gill, Rev. Sci. Instrum. **29**, 688 (1958).
[67] Y.-Q. Song, *Nuclear Magnetic Resonance Imaging in Chemical Engineering*, edited by S. Han and S. Stapf (Wiley-VCH, Weinheim, 2005).
[68] P. N. Sen, Concepts Magn. Reson. **23A**, 1 (2004).
[69] M. D. Hürlimann, L. Venkataramanan, C. Flaum, P. Speier, C. Karmonik, R. Freedman, and N. Heaton, Proceedings of the 43rd Annual SPWLA Meeting Oiso, Japan, 2002, Paper No. FFF.
[70] M. Hurlimann, L. Burcaw, and Y.-Q. Song, J. Colloid Interface Sci. **297**, 303 (2005).
[71] P. J. McDonald, J.-P. Korb, J. Mitchell, and L. Monteilhet, Phys. Rev. E **72**, 011409 (2005).
[72] L. Monteilhet, J.-P. Korb, J. Mitchell, and P. J. McDonald, Phys. Rev. E **74**, 061404 (2006).
[73] J.-H. Lee, C. Labadie, C. S. Springer, Jr., and G. S. Harbison, J. Am. Chem. Soc. **115**, 7761 (1993).
[74] P. L. Hubbard, K. M. McGrath, and P. T. Callaghan, Langmuir **21**, 4340 (2005).
[75] K. E. Washburn and P. T. Callaghan, Phys. Rev. Lett. **97**, 175502 (2006).
[76] J. J. Attard, S. J. Doran, N. J. Herrod, T. A. Carpenter, and L. D. Hall, J. Magn. Reson. **96**, 514 (1992).
[77] J. J. Attard, T. A. Carpenter, L. D. Hall, S. Davies, M. J. Taylor, and K. J. Packer, Magn. Reson. Imaging **9**, 815 (1991).
[78] P. J. Barrie, Annu. Rep. NMR Spectrosc. **41**, 265 (2000).
[79] G. C. Borgia, A. Brancolini, A. Camanzi, and G. Maddinelli, Magn. Reson. Imaging **12**, 221 (1994).
[80] S. Chen, F. Qin, K.-H. Kim, and A. T. Watson, *Proceedings of the 67th Annual Technology Conference of the Society of Petroleum Engineers*, Paper No. 24760 (1992), pp. 1013–1026.
[81] W. A. Edelstein, H. J. Vinegar, P. N. Tutunjian, P. B. Roemer, and O. M. Mueller, *Proceedings of the 63rd Annual Technology Conference of the Society of Petroleum Engineers*, Paper No. 18272 (1988), pp. 101–112.
[82] M. K. Gingras, B. MacMillan, B. J. Balcom, T. Saunders, and S. G. Pemberton, J. Sediment Res. **72**, 552 (2002).
[83] G. Guillot, C. Chardaire–Riviere, S. Bobroff, A. Le Roux, J. C. Roussel, and L. Cuiec, Magn. Reson. Imaging **12**, 365 (1994).
[84] G. J. Hirasaki, *NMR Imaging in Chemical Engineering*, edited by S. Stapf and S.-I. Han (Wiley-VCH, Weinheim, 2006).
[85] M. R. Merrill, Appl. Magn. Reson. **5**, 307 (1993).
[86] A. E. Pomerantz, E. E. Sigmund, and Y.-Q. Song, Appl. Magn. Reson. **32**, 221 (2007).
[87] E. H. Isaaks and R. M. Srivastava, *An Introduction to Applied Geostatistics* (Oxford University Press, New York, 1989).
[88] A. N. Tikhonov and V. Y. Arsenin, *Solutions of Ill-Posed Problems* (Wiley, New York, 1977).
[89] J. Skilling, *Maximum Entropy and Bayesian Methods*, edited by J. Skilling (Kluwer Academic, Dordrecht, 1989), pp. 45–52.
[90] C. L. Lawson and R. J. Hanson, *Solving Least Squares Problems* (Prentice-Hall, Englewood Cliffs, NJ, 1974).
[91] E. J. Fordham, A. Sezginer, and L. D. Hall, J. Magn. Reson., Ser. A **113**, 139 (1995).
[92] R. M. Kroeker and R. M. Henkelman, J. Magn. Reson. **69**, 218 (1986).
[93] G. C. Borgia, R. J. S. Brown, and P. Fantazzini, J. Magn. Reson. **132**, 65 (1998).
[94] Y.-Q. Song, L. Venkataramanan, and L. Burcaw, J. Chem. Phys. **122**, 104104 (2005).
[95] R. Parker and Y.-Q. Song, J. Magn. Reson. **174**, 314 (2005).
[96] Y.-Q. Song, Magn. Reson. Imaging **25**, 445 (2007).
[97] L. Venkataramanan, Y.-Q. Song, and M. D. Hürlimann, IEEE Trans. Signal Process. **50**, 1017 (2002).
[98] J. P. Butler, J. A. Reeds, and S. V. Dawson, SIAM (Soc. Ind. Appl. Math.) J. Numer. Anal. **18**, 381 (1981).
[99] R. J. S. Brown, Concepts Magn. Reson. **13**, 344 (2001).
[100] J. Jackson, L. Burnett, and J. Harmon, J. Magn. Reson. **41**, 411 (1980).
[101] K. Turco, J. Brenneke, S. Jebutu, A. Kirkwood, H. Thern, and R. Chemali, Proceedings of the SPWLA 48th Annual Logging Symposium, 2007, Paper No. OOO.
[102] S. Shtrikman and Z. Taicher, U.S. Patent No. 4,710,713 (December 1, 1987).
[103] M. G. Prammer, J. Bouton, R. N. Chandler, E. D. Drack, and M. N. Miller, Proceedings of the 73th Annual SPE Technical Conference and Exhibition, Dallas, 1998 (unpublished), Paper No. SPE-49011.
[104] R. L. Kleinberg, A. Sezginer, D. D. Griffin, and M. Fukuhara, J. Magn. Reson. **97**, 466 (1992).
[105] M. Klein, R. Fechete, D. E. Demco, and B. Blümich, J. Magn. Reson. **164**, 310 (2003).
[106] D. Rata, F. Casanova, J. Perlo, D. Demco, and B. Blümich, J. Magn. Reson. **180**, 229 (2006).
[107] J. Perlo, F. Casanova, and B. Blumich, J. Magn. Reson. **166**, 228 (2004).
[108] J. Perlo, F. Casanova, and B. Blumich, J. Magn. Reson. **176**, 64 (2005).
[109] B. Manz, A. Coy, R. Dykstra, C. D. Eccles, M. W. Hunter, B. J. Parkinson, and P. T. Callaghan, J. Magn. Reson. **183**, 25 (2006).
[110] P. McDonald, P. Aptaker, J. Mitchell, and M. Mulheron, J. Magn. Reson. **185**, 1 (2007).
[111] A. Marble, I. Mastikhin, B. Colpitts, and B. Balcom, J. Magn. Reson. **183**, 228 (2006).
[112] P. Prado, B. Blumich, and U. Schmitz, J. Magn. Reson. **144**, 200 (2000).
[113] M. W. Hunter, P. T. Callaghan, R. Dykstra, C. D. Eccles, and S. Vamanan, Magn. Reson. Imaging **23**, 407 (2005).

[114] W.-H. Chang, J.-H. Chen, and L.-P. Hwang, Magn. Reson. Imaging **24**, 1095 (2006).
[115] S. Rahmatallah, Y. Li, H. C. Seton, I. Mackenzie, J. S. Gregory, and R. Aspden, J. Magn. Reson. **173**, 23 (2005).
[116] K. R. Brownstein and C. E. Tarr, Phys. Rev. A **19**, 2446 (1979).
[117] H. C. Torrey, Phys. Rev. **104**, 563 (1956).
[118] L. J. Zielinski, Y.-Q. Song, S. Ryu, and P. N. Sen, J. Chem. Phys. **117**, 5361 (2002).